Science Signaling
AAAS

www.sciencesignaling.org/cgi/content/full/5/205/ra2/DC1

Supplementary Materials for

Incoherent Feedforward Control Governs Adaptation of Activated Ras in a Eukaryotic Chemotaxis Pathway

Kosuke Takeda, Danying Shao, Micha Adler, Pascale G. Charest, William F. Loomis, Herbert Levine, Alex Groisman, Wouter-Jan Rappel,* Richard A. Firtel*

*To whom correspondence should be addressed. E-mail: rappel@physics.ucsd.edu (W.-J.R.); rafirtel@ucsd.edu (R.A.F.)

Published 3 January 2012, *Sci. Signal.* **5**, ra2 (2012)
DOI: 10.1126/scisignal.2002413

The PDF file includes:

Text S1. Effects of two species of receptors.

Our model included two populations with different receptor affinities. Including only one population led to a dose-response curve that fit less accurately with the experimental results. This is demonstrated in fig. S4, in which we show the results of our simulations if only the low affinity (dashed lines) or the high affinity receptor population (dotted lines) was included. As a comparison, we also plotted our simulations results for the two-population receptor model. Inclusion of only the low affinity receptors led to a reduced response for small values of the stimulus in the non-pretreated cells. The effect of only high affinity receptors was more pronounced, because it increased the response at low values in the non-pretreated cells. Furthermore, it greatly reduced the response in cells that were pretreated with 100 nM cAMP.

We also calculated the Akaike's information criterion, AIC, a measure of the relative goodness of fit. This criterion is expressed as $AIC = 2k + \chi^2$, where k is the number of fitting parameters. We found the following values for this criterion: AIC=20.5 (for the model with both receptor populations), AIC=31 (with only the receptors with K_d=60 nM), and AIC=17.5 (with only the receptors with K_d=450 nM). This indicates that a model with either both or only the low affinity receptors gives a better a fit than the model with only the high affinity receptors.

Text S2. Model equations.

If we assume that the cytosolic concentration of all components is uniform, we can cast the incoherent feed forward model and the integral control model in terms of a set of coupled ordinary differential equations (ODEs). These equations, which describe the dynamics of the concentrations of the components, can then be easily integrated to determine the dynamics of the various components. For the incoherent feedforward model, the equations take on the form:

$$\frac{dR_1}{dt} = k_{R1}(cAMP + r_1)(R_1^{tot} - R_1) - k_{-R1}R_1$$
$$\frac{dR_2}{dt} = k_{R2}(cAMP + r_2)(R_2^{tot} - R_2) - k_{-R2}R_2$$
$$R = R_1 + R_2$$
$$\frac{dGEF}{dt} = k_{GEF}R - k_{-GEF}GEF$$
$$\frac{dGAP}{dt} = k_{GAP}R - k_{-GAP}GAP$$
$$\frac{dRas^{GTP}}{dt} = k_{Ras}GEF(Ras^{tot} - Ras^{GTP}) - k_{-Ras}GAP\,Ras^{GTP}$$
$$\frac{dRBD^{cyt}}{dt} = k_{RBD}^{off}(RBD^{tot} - RBD^{cyt}) - k_{RBD}^{on}Ras^{GTP}RBD^{cyt}$$

The first two equations describe the binding process of the external chemoattractant, cAMP, to the two receptor populations, R_1 and R_2. One population has a large K_d value and one has a small K_d value. The downstream activity of the bound receptors is assumed to be the same for both populations, such that the effective input in the equations for the downstream components is simply the sum, R. Also, we have allowed for the possibility of constitutive activation, parameterized through r_1 and r_2. The fourth and fifth equations describe the first order activation and deactivation of RasGEF and RasGAP (denoted for brevity by *GEF* and *GAP*), and the sixth equation models the dynamics of activated Ras, denoted here as Ras^{GTP}. The total concentration of Ras is given by Ras^{tot}. The final equation describes the cytosolic reporter molecule RBD-GFP, denoted by RBD^{cyt}. Its total concentration is RBD^{tot} and it binds membrane-bound activated Ras, leading to a removal from the cytosol, and is removed from the membrane with simple first order kinetics.

The equations for the integral control model are identical to the ones above, with the equation for RasGAP replaced by $\frac{dGAP}{dt} = k_{GAP}Ras^{GTP} - k_{-GAP}$. This form of the equations contains a zero-order term, and can be derived from the full Michaelis-Menten kinetic equations assuming saturation conditions (see also below) (*1*). We have verified through direct simulations that the system with full Michaelis-Menten kinetics or first order kinetics shows quantitatively similar behavior. In addition, we verified that

including a feedback loop from Ras to RasGEF, as suggested in previous studies (*2*), does not change the qualitative results of the model.

Text S3. Data fitting.

To fit the experimental data, we chose 21 discrete experimental points that best characterized the experimental data set. Specifically, we chose 5 points from the dose response curve for the non-pretreated cells but excluded the response of non-pretreated cells to a 1 μM stimulus because we used this value to normalize our results. Furthermore, we picked the 3 points of the dose-response curve for cells pretreated with 100 nM cAMP (Fig. 2C). The fit also used the equivalent 8 points of the time response curves (Fig. 2D). The resulting 16 points were supplemented by 5 points from the 2 experiments shown in Fig. 2, E and F, (0 to 0.2 nM, followed by 0 nM and 100 nM to 1 μM, followed by 100 nM). These were the peak amplitudes, estimated to be 1.0905 and 1.1196, and peak times, taken to be 19.5 sec and 8 sec, following a decrease in the cAMP concentration. Finally, the last point used in our fit was the amplitude of the response 60 sec after a change in concentration from 0.2 nM to 0, estimated to be equal to 1 (Fig. 2E).

Our model contains 18 parameters, of which we fixed 9: We chose the off rates of the 2 receptors populations to be equal to the values found in single molecule experiments (*3*): k_{-R1}=0.16 s^{-1} and k_{-R2}=1.1 s^{-1}. Furthermore, we fixed k_{R1} and k_{R2} by taking the disassociation constant for the high affinity receptor population to be 60 nM and for the low affinity population to be 450 nM, consistent with experimental values(*4*). We further reduced the number of free parameters by noticing that k_{GEF} did not affect the kinetics of GEF activation and was related only to the amount of GEF, which regulates Ras activation. Because k_{Ras} also regulates activation of Ras, we simply took $k_{GEF}=0.1k_{-GEF}$. Similarly, we fixed $k_{GAP}=0.1k_{-GAP}$. Moreover, because k_{-GAP} should always be smaller than k_{-GEF}, and because the system is primarily sensitive to the ratio of the two parameters, we used $ln(k_{-GEF}/k_{-GAP})$ instead of k_{-GAP} as a fitting parameter. Finally, we normalized the Ras and RBD concentrations so that Ras^{tot}=1 and RBD^{tot}=1.

The model equations were integrated in time until a steady state was obtained. The resulting numerical values of the N=21 fit points, x_i^{sim}, were then compared to the experimental values, $x_i^{\exp}$, using the following error function

$$E = \frac{1}{N}\sum_{i=1}^{21}\left(\frac{x_i^{sim} - x_i^{\exp}}{\sigma_i^{\exp}}\right)^2 ,$$

where σ_i^{exp} (i=1,2,…,21) are standard deviations of the experimental data for each fit point. The task is to search for the parameter set **k** that minimizes *E*: $\mathbf{k} = \arg\min_{\mathbf{k}}(E)$.

Because the resulting 9-dimensional parameter space can have numerous local minima, we chose simulated annealing as our method of fitting. Unlike other algorithms, simulated annealing samples a large region of parameter space and does not reject parameter choices that do not improve the fit (*5*). This is done by assigning an artificial temperature and “cooling” the system. Specifically, we started from a high temperature (T=3000), performed 100 parameter searches at each iteration and reduced the

temperature by 10% after each iteration. Our program ended when the step size in the parameter space became smaller than a defined cut-off value or when the temperature had been decreased for 100 times, whichever came first. To enlarge the searchable area in parameter space, we started the program from different initial conditions. The resulting parameters, corresponding to a fit with E=0.12, are shown in Table S1.

We have also performed fits using different experimental data points and slightly different versions of the model equations. For example, in one fit we used all the data from Fig. 2, C to F, whereas in another fit, we excluded the possibility of constitutive activation of the receptors (such that r_1=0 and r_2=0). These fits still duplicated the experimental data well, with an error function that was less that 0.3. Furthermore, the parameters that were selected were always close to the ones shown in Table S1, indicating that our fitting was not very sensitive to the choice of fit points or the specific details of the model. This was not surprising, because the experimental data put considerable constraints on the possible range of the parameters. In particular, the observed transient depletion of the cytosol following an increase in chemoattractant required that k_{-GEF} was always larger than k_{-GAP}. Furthermore, k_{-GAP} determined the time scale of the return to basal amount and was thus constrained by the experimentally observed values. Also, the peak amplitude of the response limited the allowed ratios of k_{-GAP} and k_{-GEF}. Finally, the fraction of low affinity receptors, R_2^{tot}, needed to be large because cells pre-treated with 100 nM of chemoattractant showed a substantial response.

Text S4. Analytical analysis of the incoherent feedforward and the integral control topologies.

The core of the incoherent feedforward model can be represented by Fig. S8A, where the input signal *S* activates both *A* and *B*, which control the dynamics of the output *X*. The equations describing this core motif can be written as

$$\frac{dA}{dt} = k_a S - k_{-a} A \qquad (1)$$

$$\frac{dB}{dt} = k_b S - k_{-b} B \qquad (2)$$

$$\frac{dX}{dt} = k_x A(1 - X) - k_{-x} BX \qquad (3)$$

where we normalized the *X* equation by the total amount of *X*. The steady state values of A and B depend on S, $A_0 = \frac{k_a}{k_{-a}} S,\ B_0 = \frac{k_b}{k_{-b}} S$, whereas the steady state amount of *X* is $X_0 = \frac{k_x A_0}{k_x A_0 + k_{-x} B_0}$. Thus, because both A_0 and B_0 depend linearly on *S*, X_0 will be independent of S. A linear stability analysis for the steady state of the system can be carried out. The growth mode λ is given by the solution of the following eigenvalue problem:

$$\begin{vmatrix} -k_{-a} - \lambda & 0 & 0 \\ 0 & -k_{-b} - \lambda & 0 \\ k_x(1 - X_0) & -k_{-x} X_0 & -k_x A_0 - k_{-x} B_0 - \lambda \end{vmatrix} = 0$$

These eigenvalues are always real and negative, demonstrating that the steady state is linearly stable and that *X* does not exhibit oscillations.

The kinetics of *X* depends on the amount of *A* and *B* present. For small values of *S*, both *A* and *B* are small and the kinetics of *X* is slow. That is, Eqn.(1) and Eqn.(2) are much faster than Eqn.(3) and we can approximate *A* and *B* by their quasi-steady state values: $A \sim \frac{k_a}{k_{-a}} S, B \sim \frac{k_b}{k_{-b}} S$. Then, Eqn.(3) can be written as

$$\frac{1}{S}\frac{dX}{dt} = \frac{k_x k_a}{k_{-a}}(1 - X) - \frac{k_{-x} k_b}{k_{-b}} X$$

Thus, the timescale of recovery for *X*, τ, is inversely proportional to the signal strength, $\tau \sim 1/S$. On the other hand, when *S* is large, Eqn.(3) equilibrates quickly and

$X \sim \frac{k_x A}{k_x A + k_{-x} B}$. Because both *A* and *B* are linearly dependent on *S*, $A = \frac{k_a}{k_{-a}} S(1 - e^{-k_{-a} t})$ and $B = \frac{k_b}{k_{-b}} S(1 - e^{-k_{-b} t})$, we find that the kinetics of *X* are independent of *S*.

The integral control models, with negative feedback, can be represented by two core motifs. For analytical convenience, we assume that the activation of activator *A* is fast compared to the timescales for *B* and *X*. Then, these motifs reduce to two-node topologies and in the first one (Fig. S8B), the buffering node is activated by *X* and deactivates *X*:

$$\frac{dX}{dt} = k_x S(1 - X) - k_{-x} BX \qquad (4)$$

$$\frac{dB}{dt} = k_b X - k_{-b} \qquad (5)$$

The zero-order terms in these equations, and in the ones for the second motif below were chosen to facilitate the analytical treatment and can be derived in certain limits of the full Michaelis-Menten kinetic equations (*1*). We have verified through numerical simulations that the system with full Michaelis-Menten dynamics shows qualitatively similar behavior.

The steady state amounts are $X_0 = \frac{k_{-b}}{k_b}$ and $B_0 = \frac{k_x S(1 - X_0)}{k_{-x} X_0}$. A linearization around these steady state values gives as the growth modes:

$$\begin{vmatrix} -k_x S - k_{-x} B_0 - \lambda & -k_{-x} X_0 \\ k_b & -\lambda \end{vmatrix} = 0 \qquad \Rightarrow \qquad \lambda^2 + (k_x S + k_{-x} B_0)\lambda + k_{-x} k_{-b} = 0$$

Imaginary values for these modes will result in oscillations in the value of *X* for constant *S*. To avoid these oscillations, one has to choose a small enough value for k_{-b}. Of course, it might also possible to suppress these oscillations through additional loops in the network.

When Eqn. (4) is much faster than Eqn. (5), we can approximate *B* by its quasi-steady state value $B \sim \frac{k_x S(1 - X)}{k_{-x} X}$. Then, $\frac{dB}{dt} = -\frac{k_x S}{k_{-x} X^2} \frac{dX}{dt} = k_b X - k_{-b}$ and

$$S \frac{dX}{dt} = -\frac{k_{-x}}{k_x} X^2 (k_b X - k_{-b})$$

Thus, the recovery time scale τ increases with S: $\tau \sim S$, inconsistent with the experimental results.

In the second motif (Fig. S8C), the buffering node *B* activates *X* and is deactivated by *X*. Because *B* is not activated by the signal, we will assume a constant constitutive activation:

$$\frac{dX}{dt} = k_x(S+c)B(1-X) - k_{-x}X \qquad (6)$$

$$\frac{dB}{dt} = k_b - k_{-b}X \qquad (7)$$

with steady-state values $X_0 = \frac{k_b}{k_{-b}}$ and $B_0 = \frac{k_{-x}\frac{k_b}{k_{-b}}}{k_x(S+c)(1-\frac{k_b}{k_{-b}})}$

The linear stability is found by solving $\begin{vmatrix} -\frac{k_{-x}}{1-\frac{k_b}{k_{-b}}} - \lambda & k_x(S+c)(1-\frac{k_b}{k_{-b}}) \\ -k_{-b} & -\lambda \end{vmatrix} = 0$,

leading to $\lambda^2 + \frac{k_{-x}}{1-\frac{k_b}{k_{-b}}}\lambda + k_x(S+c)(k_{-b}-k_b) = 0$. Thus, again, the kinetics of the buffering node B, characterized by k_{-b}, needs to be slow to avoid oscillations. Then, Eqn.(6) will equilibrate quickly, and $X \approx \frac{k_x(S+c)B}{k_x(S+c)B + k_{-x}}$. For large values of *S*, X reaches its peak $X_{peak} \approx 1$ (Fig. S6G) and remains saturated for a prolonged period. During this time, the decay rate of B is about $\frac{dB}{dt} \approx k_b - k_{-b}$, leading to

$$\frac{dX}{dt} \approx \frac{k_x k_{-x}(S+c)}{[k_x(S+c)B + k_{-x}]^2}\frac{dB}{dt} \approx \frac{k_x k_{-x}(S+c)}{[k_x(S+c)B_0 + k_{-x}]^2}(k_b - k_{-b}).$$

The saturation time can be estimated to be $T_{saturation} \approx \frac{B_{0,pre}}{k_{-b} - k_b}$ where $B_{0,pre}$ is the steady state value of B before the stimulus step.

Text S5. Spatially extended models.

A spatially extended version of the adaptation model can be formulated in a straightforward manner. In this spatially extended version of the LEGI model, both *GAP* and RBD^{cyt} diffuse in the cytosol with diffusion constants D_{GAP} and D_{RBD}, respectively. The above equations for the receptors and *GEF* are unchanged and the remaining equations now describe the concentration in the cytosol and on the membrane in terms of partial different equations (PDEs):

$$\frac{dGAP^{mem}}{dt} = k_{GAP}^{on} GAP^{cyt} - k_{-GAP} GAP^{mem}$$

$$\frac{\partial GAP^{cyt}}{\partial t} = D_{GAP} \nabla^2 GAP^{cyt}$$

$$\frac{dRas^{GTP}}{dt} = k_{Ras} GEF(Ras^{tot} - Ras^{GTP}) - k_{-Ras} GAP^{mem} Ras^{GTP}$$

$$\frac{dRBD^{mem}}{dt} = k_{RBD}^{on} Ras^{GTP} RBD^{cyt} - k_{RBD}^{off} RBD^{mem}$$

$$\frac{\partial RBD^{cyt}}{\partial t} = D_{RBD} \nabla^2 RBD^{cyt}$$

These equations need to be supplemented with the boundary conditions

$$D_{GAP} \frac{\partial GAP^{cyt}}{\partial n} = k_{GAP} R - k_{GAP}^{on} GAP^{cyt}$$

$$D_{RBD} \frac{\partial RBD^{cyt}}{\partial n} = -k_{RBD}^{on} Ras^{GTP} RBD^{cyt} + k_{RBD}^{off} RBD^{mem}$$

where *n* is the normal to the cell membrane.

We have simulated these equations, representing a spatially extended implementation of the LEGI model (*6*), using a disk-shaped cell with radius R=5 μm. The resulting RBD^{cyt} dynamics, following an increase in cAMP, is shown in Fig. S9 as symbols. The corresponding RBD^{cyt} dynamics for the case where the cytosolic RBD-GFP concentration is assumed to be uniform and the equations can be described by ODEs is plotted as a solid line. A comparison reveals that both models display the same quantitative behavior. Of course, this result is not surprising because, as long as D_{RBD} is large enough, the spatial variations of RBD^{cyt} will be negligible.

Fig. S1: Detailed drawing of the microfluidic device

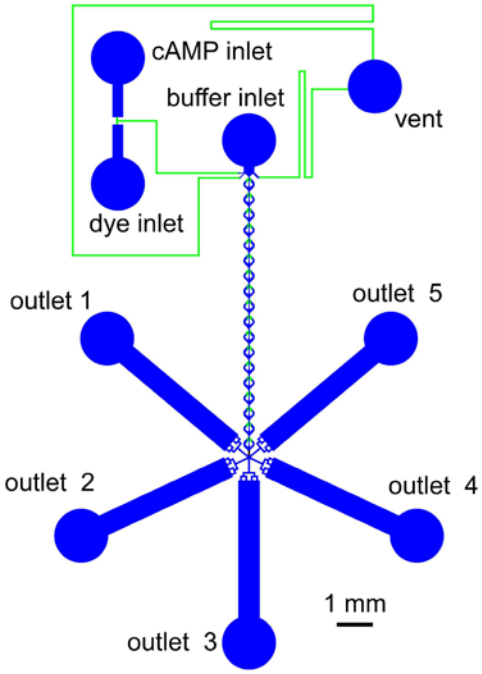

A detailed drawing of microchannels in the microfluidic device used in this study. Microchannels with depths of 30 and 120 µm are shown in green and blue, respectively. Circles mark the inlet and outlet ports. The device consisted of a chip made of polydimethylsiloxane (PDMS), with microchannels engraved on its surface, and a cover glass sealing the microchannel. The chip was cast of PDMS using a master mold fabricated with standard UV photolithography. A 5 inch silicon wafer was spin-coated with a 30 µm of a UV-curable epoxy (SU8-2015 by Microchem), exposed to UV-light through a photomask, spin-coated with another layer of epoxy to a total thickness of 120 µm, exposed to UV-light through another photomask, and developed. The microfluidic device had three inlets: for a buffer, a concentrated solution of cAMP, and a solution of fluorescent dye (Alexa 594). The device also had a vent and five outlets. The microchannel network of the device consisted of 30 µm and 120 µm deep channels. Its major elements were 5 observation chambers, each situated upstream of a dedicated outlet, a mixing channel, and resistance channels. At its upstream end, the mixing channel was connected to the three inlets, and at its downstream end the mixing channel was connected to the 5 observation chambers. The mixing channel was a modification of a previous design (*7*) and consisted of a chain of 18 identical segments with 30 and 120 µm deep elements that generated a three-dimensional flow with stretching and folding that promoted efficient mixing.

The flow in the device was driven by the application of differential pressures between the inlets and outlets of the device. The pressures were controlled either hydrostatically, by setting certain height differences between the reservoirs feeding the inlets and the reservoirs connected to the outlets and the vent, or by pressurizing the inlet reservoirs with compressed air supplied by an accurate regulator (8310 by Porter Instruments) with the pressure measured by a sensitive electronic gauge (Cecomp GPG1000B). All 5 outlets of the device were connected to a single reservoir through 5 separate lines of Tygon tubing. At any given time, the flow through 4 out of 5 outlets was blocked (by mechanically clamping the tubing lines connected to the outlets) and the entire flow through the mixing channel was directed towards a single observation chamber (and a single outlet). The microchannel network was designed such that the flow rate through an active observation chamber was set solely by the pressure at the buffer inlet that remained constant throughout an experiment. The concentration of cAMP in the active observation chamber was a linear function of the difference between the pressure at the cAMP inlet, P_c, and a certain reference pressure, P_0. At $P_c < P_0$, the entire stream of the concentrated cAMP solution was diverted towards the vent, resulting in 0 cAMP concentration in the observation chamber ($[cAMP] = 0$). At $P_c > P_0$, the concentration of cAMP in the observation chamber was $[cAMP] = \alpha[cAMP]_0(P_c - P_0)$, where $[cAMP]_0$ was the concentration of cAMP in the solution fed to the cAMP inlet. The coefficient α was equal to $1/(P_{\max} - P_0)$, where $P_{\max}$ was the pressure at which the solution in the observation chamber was the same as the solution fed to the cAMP inlet. In our experiments, the pressure at the cAMP outlet was always below this limit ($P_c < P_{\max}$).

To calibrate a device and find the values P_0 and $P_{\max}$ for the device, we used the fluorescent dye that was fed to the dye inlet. During the calibration, the dye inlet was open and pressurized and the cAMP inlet was blocked. In contrast, during the experiments on *Dictyostelium* cells, the dye inlet was blocked, whereas the cAMP inlet was open and pressurized. To change $[cAMP]$ in the active observation chamber, the pressure at the cAMP inlet was abruptly changed using pressure-regulated compressed air and a solenoid valve. The transition time for the concentration change in an observation chamber (near its upstream end) was 0.26 s based on a 10% to 90% criterion (Fig. 1B). The maximal flow velocity in an active observation chamber was 10 mm/s, corresponding in a shear stress of ~0.33 Pa at the surface of cell attached to the substratum that was expected to result in a minimal mechanical stimulation of the cells. Importantly, the flow velocity and the surface shear stress in the observation chamber remained constant when the cAMP concentration was switched, excluding any possible change in the mechanical stimulus. The availability of the 5 separate observation chambers made it possible to repeat the cell stimulation with cAMP 5 times in a single experiment, thus increasing the experimental throughput.

Fig S2. Membrane-associated RBD-GFP is inversely related to cytosolic RBD-GFP fluorescence.

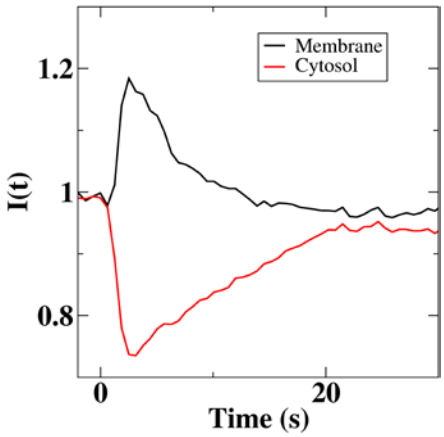

The cytosolic (red line) and the membrane fluorescence intensity following a sudden increase in chemoattractant concentration at t=0 s.

Fig. S3. Responses in latrunculin-treated cells.

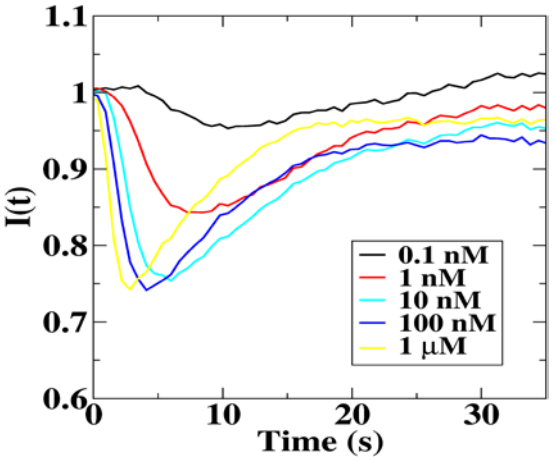

We quantified the degree of adaptation of Ras-GTP in cells treated with 15 μM latrunculin B by exposing previously unstimulated cells to different chemoattractant concentrations, ranging from 1.0×10^{-2} to 1.0×10^{3} nM in 10-fold increments. The RBD-GFP cytosolic fluorescence intensity I(t) as a function of time in cells treated with the 5 highest chemoattractant concentrations are shown. As in the case for cells not treated with latrunculin B (Fig. 2A), the response increases for increasing concentrations and the peak time, T_{peak}, decreases with increasing concentration.

Fig. S4. Effects of different receptor populations.

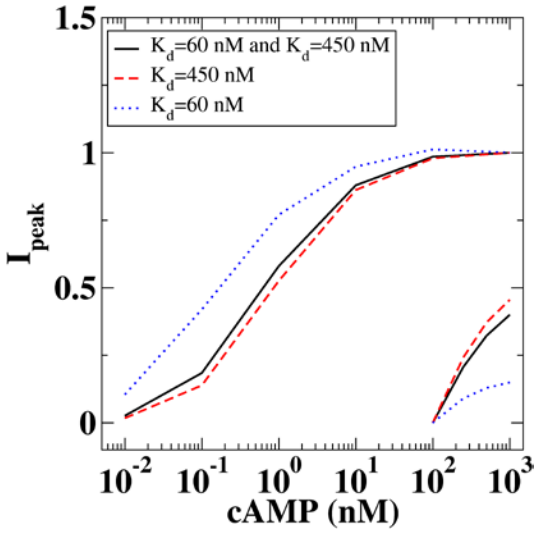

Numerical dose response curves for cells with only low affinity (K_d=450 nM; red dashed lines) or only high affinity (K_d=60 nM; blue dotted lines) receptors. Shown are the results without any pre-stimulus and with pre-stimulation with 100 nM chemoattractant. The solid curves are shown for comparison and represent the results of simulations with the mixed receptor population described in the main text.

Fig. S5. Response times for the different models.

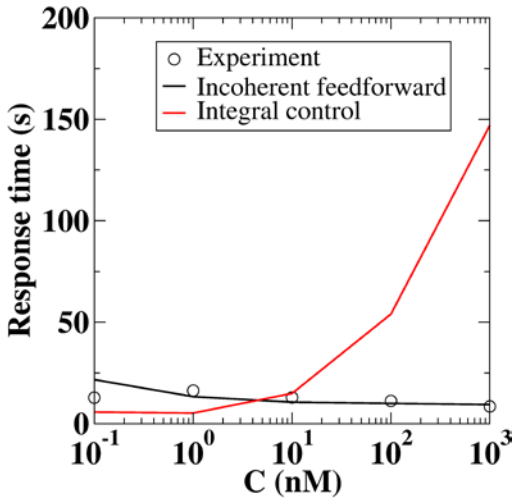

We defined the response time for the integral control and the incoherent feedforward model as the time between the half-peak value during the rise phase and the half-peak value during the decay phase of the response. In the integral control model, this response time increased as the stimulus size was increased (red line). In contrast, the response time decreased for increasing step sizes in the incoherent feedforward model (black line), consistent with experimental results (symbols).

Fig. S6. Possible integral control topologies.

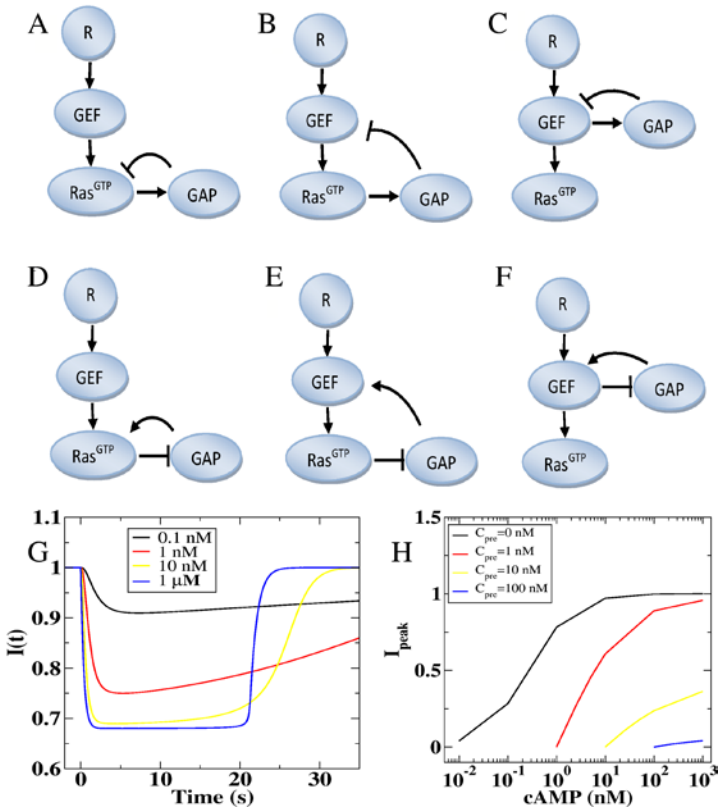

(**A** to **H**) All possible three-node topologies containing a negative feedback loop (integral control topologies), including ones that are biologically not plausible. The dynamics of topologies (B) and (C) are qualitatively similar to the one depicted in A and are discussed in the main text. In the topologies of (A), (B), and (C), either RasGEF or activated Ras activates RasGAP which, in turn, exerts negative feedback. Through explicit numerical simulations, we have verified that these three topologies are inconsistent with the experiments for the reasons described in the main text: The timescale of the return to basal amount following an increase in cAMP is proportional to the magnitude of the stimulus. The qualitative dynamics of topologies (D) to (F) are shown in (G) and the corresponding dose-response curves are plotted in (H). The topologies of (D) to (F) have an inhibitory coupling between either RasGEF or activated Ras and RasGAP. The feedback loop is closed through a positive link between RasGAP and RasGEF or activated Ras. These topologies are also inconsistent with the experimental findings. In particular, for large values of the stimulus, Ras-GTP saturates and remains close to its maximal

value for a prolonged period of time (G). This would result in experiments with a prolonged plateau in the RBD-GFP intensity. Furthermore, the saturability of Ras-GTP makes it impossible to obtain the dynamic range observed in the dose-response experiments. Specifically, it is possible to obtain a dose-response curve that is close to the experimental one for untreated cells. However, because for large values of the chemoattractant concentration Ras-GTP is saturated, the response to an increased stimulus of cells that were pre-treated with a large chemoattractant concentration is small. This is shown in (H), in which we plot the dose-response curves for different values of initial chemoattractant concentrations. There is a small response of cells pre-treated with 100 nM chemoattractant (blue line) to subsequent increases in chemoattractant concentrations, inconsistent with the experimental results.

Fig. S7. Possible incoherent feedforward topologies.

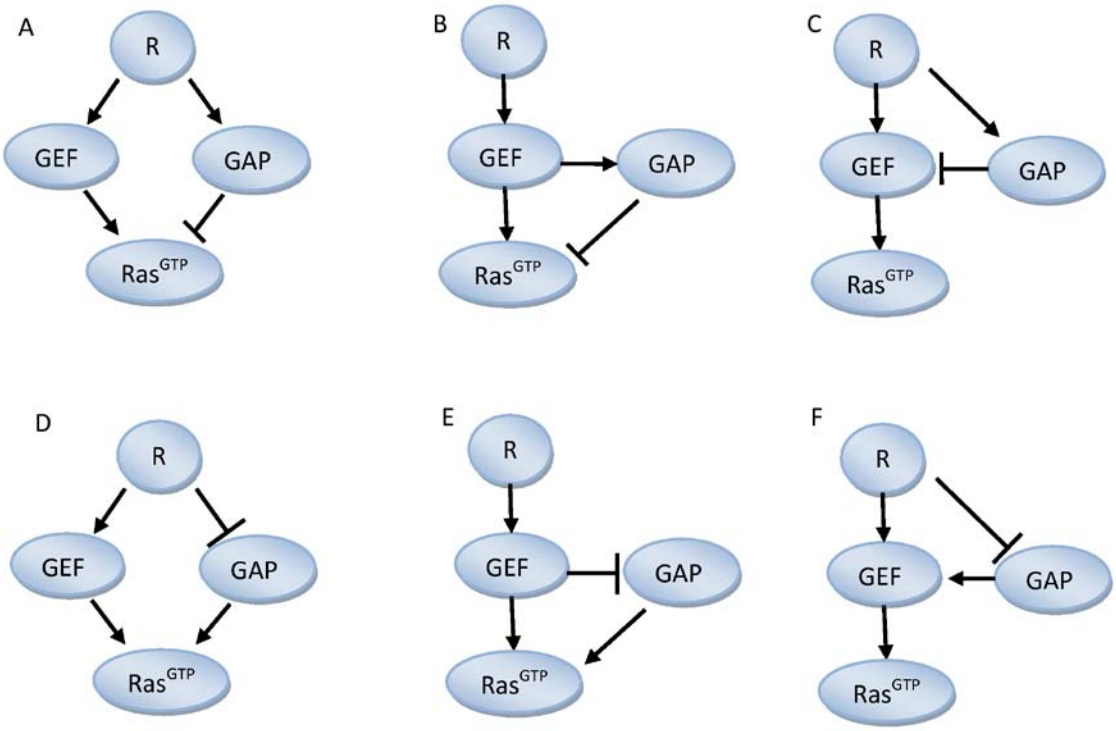

Theoretically possible implementations, including ones that are biologically not plausible, of the incoherent feedforward model. The topology in (A) is the one considered in this study.

Fig. S8. Core model topologies.

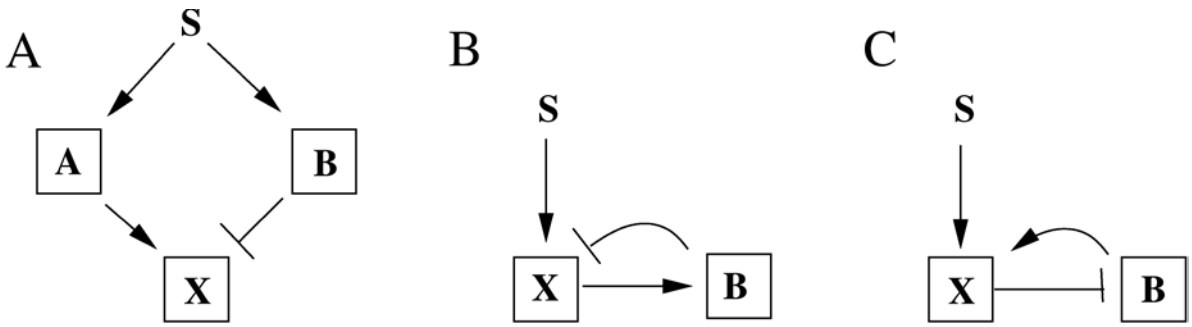

Basic motifs of incoherent feedforward model (A) and integral control (negative feedback) model [(B) and (C)]. S is the input signal, and X is the output.

Fig. S9. Comparison of the response in a spatially uniform and spatially extended model.

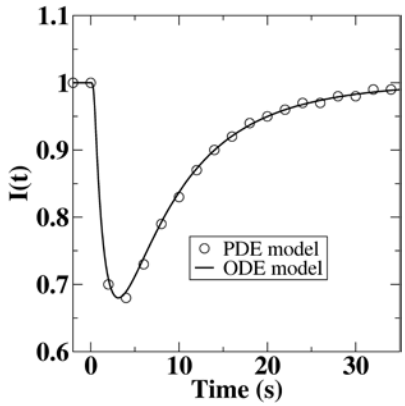

The intensity of cytosolic RBD-GFP, normalized by RBD^{cyt} before simulation, as a function of time following a sudden increase in chemoattractant from 0 to 1 μM for the spatially uniform model governed by ODEs (solid line) and the spatially extended model described by PDEs (symbols). The common parameters for both models are given in Table S1 and the additional parameters for the spatially extended model are: $D_{GAP}=30\mu m^2/s$, $D_{RBD}=10\mu m^2/s$, $k_{GAP}^{on}=3\mu m/s$.

Table S1. Model parameters used in this study.

parameter	value	parameter	value
R_1^{tot}	0.1	k_{-GEF}	0.4 sec^{-1}
R_2^{tot}	0.9	k_{GAP}	0.01 sec^{-1}
k_{R1}	0.00267 $nM^{-1}sec^{-1}$	k_{-GAP}	0.1 sec^{-1}
k_{-R1}	0.16 sec^{-1}	Ras^{tot}	1
k_{R2}	0.00244 $nM^{-1}sec^{-1}$	k_{Ras}	390 sec^{-1}
k_{-R2}	1.1 sec^{-1}	k_{-Ras}	3126 sec^{-1}
r_1	0.012 nM	RBD^{tot}	1
r_2	0.115 nM	k_{RBD}^{off}	0.53 sec^{-1}
k_{GEF}	0.04 sec^{-1}	k_{RBD}^{on}	1.0 sec^{-1}

References

1. W. Ma, A. Trusina, H. El-Samad, W. A. Lim, C. Tang, Defining network topologies that can achieve biochemical adaptation. *Cell* **138**, 760 (Aug 21, 2009).
2. J. Das *et al.*, Digital signaling and hysteresis characterize ras activation in lymphoid cells. *Cell* **136**, 337 (Jan 23, 2009).
3. M. Ueda, Y. Sako, T. Tanaka, P. Devreotes, T. Yanagida, Single-molecule analysis of chemotactic signaling in Dictyostelium cells. *Science* **294**, 864 (2001).
4. P. J. M. van Haastert, R. J. W. de Wit, Demonstration of receptor heterogeneity and affinity modulation by nonequilibrium binding experiments. The cell surface cAMP receptor of Dictyostelium discoideum. *J. Biol. Chem.* **259**, 13321 (1984).
5. W. H. Press, S. A. Teukolsky, W. T. Vetterling, B. P. Flannery, *Numerical Recipes: The Art of Scientific Computing*. (Cambridge University Press, ed. 3rd, 2007), pp. 1256.
6. C. A. Parent, P. N. Devreotes, A cell's sense of direction. *Science* **284**, 765 (1999).
7. C. Simonnet, A. Groisman, Chaotic mixing in a steady flow in a microchannel. *Phys Rev Lett* **94**, 134501 (Apr 8, 2005).